DESCRIPTION OF AN INCOMPRESSIBLE VARIABLE DENSITY APPRACH FOR THE DESCRIPTION OF SUPERCRITICAL FLUID FLOWS

SPACE PROPULSION 2022
ESTORIL, PORTUGAL | 09 – 13 MAY 2022

Leandro Magalhães [(1)], João Cleto [(1)], André Silva [(1)], Jorge Barata [(1)]

[(1)] *LAETA-AEROG, University of Beira Interior, Covilhã 6201-001, Portugal, leandro.magalhaes@ubi.pt*

KEYWORDS: supercritical fluids, incompressible variable density approach, Liquid Rocket Engines

ABSTRACT:

The simplification of the incompressible but variable density jet is based on the visualization of data similarity. Given the initial encouraging results obtained in the past, we extend, in the present paper, this hypothesis to a broader range of conditions to ascertain its applicability and its role as an alternative to the more commonly fully-compressible formulations encountered in the literature. Transcritical and supercritical injection conditions are considered for nitrogen, which works as a surrogate for the oxygen-hydrogen mixture combination, characteristic of liquid rocket propulsion. A close agreement is found between experiments and numerical results in terms of axial profiles and jet spreading rates.

1. INTRODUCTION

The growing performance needs of rocket engines have resulted in combustion chamber conditions that exceed the critical point of both fuels and oxidizers, entering the realm of supercritical fluids. In the case of pure fluids, the critical point delimits the supercritical regime and is defined by pressure and temperature values that serve as identifiers. Any numerical effort dedicated to the successful description of supercritical fluid flows must precisely mimic thermodynamic singularities, which refer to the unique behaviour of thermodynamic characteristics at the critical point.

Further increases in pressure and temperature after the critical point is reached may cause the fluid to enter the so-called Widom region [1], which separates supercritical liquid- and gas-like behaviour. Several Widom lines [1,2] have been investigated as a result of singularities in various thermodynamic response functions. A local maxima or an inflection point might be used to describe them.

The Widom region, also known as pseudo-boiling in the literature [1], is the area where a small change in pressure or temperature causes a big response. Crossing the Widom area from liquid to gas-like conditions is analogous to a subcritical phase shift, but without the phase change and with the temperature change occurring over a restricted temperature range [1].

The simplification of the incompressible but variable-density jet is based on the visualization data's similarity. [4] examined and analyzed the theory, and the results were encouraging enough to warrant further testing in other, more general contexts. The seemingly vast range of CFD (computational fluid dynamics) codes, as detailed by [6], is misleading, since successful approaches and methodologies are utilized as nearly standard procedures.

The variable-density behaviour of supercritical jets can then be modelled using real gas relationships for density (in the form of an equation of state-EoS) and transport properties like dynamic viscosity and thermal conductivity, detailing ideal gas behaviour and departure functions to account for high-pressure effects, based on the amount of experimental evidence. In contrast, numerical modelling of supercritical fluid flows has traditionally relied on compressible solvers; however, as [7] point out, flows at such conditions fall below the significant Mach number threshold of 0.3, imposing severe restrictions on the numerical solver in combination with the low injection velocities. Variable density behaviour is, nevertheless, well-known in the literature. For example, [8] uses large eddy simulation (LES) in the nitrogen into nitrogen injection configuration, [9] recognizes the similarity to variable-density mixing in the mixing layer configuration oxygen-methane, and [10] uses direct numerical simulation (DNS) of temporal mixing layers of heptane-hydrogen should show similarities between vortex dynamics of the most unstable compressible and incompressible wavelengths.

In the present work, we consider transcritical and supercritical conditions representative of liquid propelled rocket engines' operational range. If we consider a mixture of oxygen-hydrogen injected into

the combustion chamber separately and at supercritical conditions, the resulting mixing behavior can be characterized by variations of temperature that are locally lower than the critical mixing temperature, putting the mixture in the transcritical regime, from where the conditions in the chamber could lead to an increase in the mixing temperature, eventually crossing the critical point into supercritical liquid-like conditions, be subjected to pseudo-boiling effects, and ultimately cross the Widom line into supercritical gas-like conditions.

While nitrogen is not used as a propellant in liquid rocket propulsion, its handling easiness during experimental campaigns, and the similar characteristics in relation to the mixture of oxygen-hydrogen, commonly used in liquid rocket propulsion, make it an excellent working fluid for the study of supercritical fluid behavior, without the inclusion of chemical equilibrium or combustion effects.

The experimental test conditions [1] detail the injection of nitrogen at transcritical and supercritical gas-like conditions into a chamber filled with supercritical nitrogen. An incompressible but variable density approach is employed in the study [2], which arose from the similarity of visualization data.

The remaining of the manuscript is organized as follows: The mathematical/physical models that form the foundation of the RANS technique are examined and discussed in order to determine their performance, benefits and drawbacks, and function in the whole process. Then results are presented for supercritical and transcritical conditions in terms of axial density quantities, jet spreading rates and shape of the profiles. Lastly, the main findings are summarized in the conclusions.

2. MATHEMATICAL MODEL

2.1. Fundamental Laws

The conservation principles of mass, momentum and energy per unit volume are represented in Eqs. 1, 2 and 3, respectively, following the hypothesis of incompressible but variable density flow [5] through the application of Favre averaging procedure. In Eqs. 1 to 3 x is the distance in the ith directions i and j, u the velocity, ρ the density, H the total enthalpy per unit volume, q the heat flux, τ the stress tensor and p the pressure.

$$\frac{\partial \bar{\rho}\widetilde{u_i}}{\partial u_i} = 0 \qquad \text{Eq.1}$$

$$\frac{\partial}{\partial t}(\bar{\rho}\widetilde{u_i}) + \frac{\partial}{\partial x_j}(\bar{\rho}\widetilde{u_i}\widetilde{u_j}) = -\frac{\partial \bar{p}}{\partial x_i} + \frac{\partial \overline{\tau_{ij}}}{\partial x_j} - \frac{\partial \bar{\rho}\widetilde{u_i''u_j''}}{\partial x_j} \quad \text{Eq.2}$$

$$\frac{\partial \bar{\rho}\widetilde{u_j}\widetilde{H}}{\partial x_j} = \frac{\partial \overline{\tau_{ij}u_i}}{\partial x_j} - \frac{\partial \widetilde{u_i}\bar{\rho}\widetilde{u_i''u_j''}}{\partial x_j} - \frac{\partial}{\partial x_j}(\bar{q_j} + \bar{\rho}\widetilde{u_j''h''}) \text{Eq.3}$$

Boussinesq's approximation of Eq.4 relates the Reynolds stresses with the average rate of strain, similarly to the Newtonian relationship between viscous stresses and the rate of strain. In Eq. 4 δ_{ij} is the Kronecker's delta function and μ_t the eddy viscosity.

$$-\bar{\rho}\widetilde{u_i''u_j''} = -\frac{2}{3}\rho\kappa\delta_{ij} + \mu_t\left(\frac{\partial \widetilde{u_i}}{\partial x_j} + \frac{\partial \widetilde{u_j}}{\partial x_i} - \frac{2}{3}\frac{\partial \widetilde{u_k}}{\partial x_k}\delta_{ij}\right) \quad \text{Eq.4}$$

The turbulent heat flux is modeled following Eq. 5, where Pr_t is the turbulent Prandtl number expressing the effect of momentum eddy diffusivity to that of heat, T the temperature, h the enthalpy and c_p the isobaric specific heat.

$$\bar{\rho}\widetilde{u_j''h''} = -\frac{c_p}{\text{Pr}_t}\frac{\partial \widetilde{T}}{\partial x_j} = -\frac{\mu_t}{Pr_t}\frac{\partial \widetilde{h}}{\partial x_j} \qquad \text{Eq.5}$$

Eddy viscosity results from a combination of a length (l) and velocity (q) characteristic scale, as indicated in Eq. 6. The characteristic scales are evaluated through the κ-ε turbulence model [11], where the eddy viscosity of Eq.6 is explicitly evaluated through Eq.7 and the turbulence kinetic energy (κ) and its dissipation rate (ε) are given in Eqs. 8 and 9, respectively, with production, destruction and transport terms. The remaining parameters in Eqs. 8 and 9 are tabulated constants given in Tab.1. In a preliminary study [12] several turbulence models commonly used in the modeling of subcritical flows were evaluated for supercritical conditions. These ranged from one-equation to two-equation and second-order models, where no correspondence was found between model complexity and quality of the results.

$$\mu_t = \rho l q \qquad \text{Eq.6}$$

$$\mu_t = C_\mu f_\mu \frac{\rho\kappa^2}{\varepsilon} \qquad \text{Eq.7}$$

$$\frac{\partial}{\partial x_j}(\rho u_j\kappa) = P - p\varepsilon + \frac{\partial}{\partial x_j}\left[\left(\mu + \frac{\mu_t}{\sigma_k}\right)\frac{\partial \kappa}{\partial x_j}\right] \quad \text{Eq.8}$$

$$\frac{\partial}{\partial x_j}(\rho u_j\varepsilon) = C_{\varepsilon 1}f_1\frac{\varepsilon}{\kappa}P - C_{\varepsilon 2}f_2\frac{\rho\varepsilon^2}{\kappa} + \frac{\partial}{\partial x_j}\left[\left(\mu + \frac{\mu_t}{\sigma_\varepsilon}\right)\frac{\partial \varepsilon}{\partial x_j}\right]$$
Eq.9

Table 1. κ-ε turbulence model constants [11].

Parameter	Value
σ_k	1.0
σ_ε	1.3
C_μ	0.09
$C_{\varepsilon 1}$	1.35
$C_{\varepsilon 2}$	1.8
f_1	1.0

The production term P in Eqs. 8 and 9 is given according to Eq.10.

$$P = \tau_{ij}\frac{\partial \widetilde{u_i}}{\partial x_j} \qquad \text{Eq.10}$$

The initial turbulence field namely the turbulence kinetic energy (κ_0) and its dissipation (ε_0) are set according to Eqs.11 and 12, respectively. While the turbulence intensity (I) of the experimental facility is not reported [3] a level of 5% is used, which was found to be reasonable according to preliminary calculations. Moreover, the length scale is considered to be $0.014d$, where d is the jet diameter and the velocity scale (u) equal to the jet velocity.

$$\kappa_0 = \frac{3}{2}(Iu)^2 \qquad \text{Eq.11}$$

$$\varepsilon_0 = \frac{c_\mu^{3/4}\kappa^{3/2}}{0.014d} \qquad \text{Eq.12}$$

2.2. Equation of State

The Peng-Robinson (PR) [12] equation of state (EoS) is used in the present work to close the system of equations, since it represents a compromise between simplicity, computational cost and accuracy. The PR EoS formulation is reproduced in Eq.11, where R is the universal gas constant, v_m the molar volume, a represents the molecular attractive potential and b the repulsive potential.

$$p = \frac{RT}{v_m - b} - \frac{a(T)}{v_m(v_m+b)+b(v_m-b)} \qquad \text{Eq.13}$$

The attractive potential dependence on temperature, $a(T)$, is retrieved from Eq. 14, explicit for the critical point (c) in Eq.15, while the function of the acentric factor (ω), representing the non-spherical degree of the molecules and the reduced temperature (T_r), describing the ratio between the temperature to its critical point value is given by Eq 16. Lastly the molecular repulsive potential at the critical point is evaluated according to Eq. 17.

$$a(T) = a(T_c).f(T_r, \omega) \qquad \text{Eq.14}$$

$$a(T_c) = 0.45724\frac{R^2 T_c^2}{p_c} \qquad \text{Eq.15}$$

$$f(T) = [1 + (0.37464 + 1.5422\omega - 0.26992\omega^2)(1 - \sqrt{T_r})]^2 \qquad \text{Eq.16}$$

$$b = b_c = 0.07780\frac{RT_c}{p_c} \qquad \text{Eq.17}$$

2.3. Transport Properties

Transport properties such as dynamic viscosity and thermal conductivity are evaluated following the so-called departure function formalism, in which to the ideal gas sate component are added departure functions that account for real gas effects such as in the case of viscosity and critical divergence in relation to the thermal conductivity behavior at the critical point [13].

Dynamic viscosity is retrieved following Eq.18

adding to the ideal gas component ($\mu^0(T)$) the departure real gas effect ($\mu^r(\rho_r, T_r)$). In Eqs.20 and 21, σ is the Lennard-Jones size parameter, M the molar mass, Ω the collision integral while the remaining parameters are tabulated constants [13].

$$\mu = \mu^0(T) + \mu^r(\rho_r, T_r) \qquad \text{Eq.19}$$

$$\mu^0(T) = \frac{0.0266958\sqrt{MT}}{\sigma^2\Omega(T^*)} \qquad \text{Eq.20}$$

$$\mu^r(\rho_c, T_c) = \sum_{i=1}^n N_i\tau^{t_i}\delta^{d_i}\exp(-\gamma\delta^{l_i}) \qquad \text{Eq.21}$$

Similarly, thermal conductivity is retrieved from Eq. 22, albeit the inclusion of the critical divergence term ($\lambda^c(\rho_r, T_r)$). In Eq.25 $\widetilde{\Omega}$ is a consequence of the specific heat at constant pressure and volume, where c_v, c_p and $\left(\frac{\partial\rho}{\partial p}\right)_T$ are obtained through the derivation of the Eos at specified values of density and temperature.

$$\lambda = \lambda^0(T) + \lambda^r(\rho_r, T_r) + \lambda^c(\rho_r, T_r) \qquad \text{Eq.22}$$

$$\lambda^0 = N_1\left[\frac{\eta^0(T)}{1\mu Pa.s}\right] + N_2\tau^{t_2} + N_3\tau^{t_3} \qquad \text{Eq.23}$$

$$\lambda^r = \sum_{i=4}^n N_i\tau^{t_i}\delta^{d_i}\exp(\gamma\delta^{l_i}) \qquad \text{Eq.24}$$

$$\lambda^c = \rho c_p\frac{KR_0 T}{6\pi\xi\eta(T,\rho)}(\widetilde{\Omega} - \widetilde{\Omega_0}) \qquad \text{Eq.25}$$

2.4. Thermodynamic Properties

The evaluation of thermodynamic properties is dependent upon the conversion of the EoS to a thermodynamically consistent caloric equation of state written for energy or enthalpy. Accordingly, enthalpy of a real gas is described following Eq.26, as a combination of ideal gas value and departure function, similarly to the evaluation of transport properties. The ideal gas enthalpy of Eq.27 is evaluated for nitrogen through the 7 coefficient NASA polynomials [14] with tabulated values for coefficients a_1 to a_6. Lastly, the caloric version [15] of the PR EoS is evaluated from Eqs. 28 and 29, where Z is the compressibility factor.

$$h(p,T) = h_0(T) + \int_{p_0}^p\left[\frac{1}{\rho} + \frac{T}{\rho^2}\left(\frac{\partial p}{\partial T}\right)_\rho\right]_T dp \qquad \text{Eq.26}$$

$$h_0(T) = \left(a_1 + a_2\frac{T}{2} + a_3\frac{T^2}{3} + a_4\frac{T^3}{4} + a_5\frac{T^4}{5} + \frac{a_6}{T}\right)RT \qquad \text{Eq.27}$$

$$\frac{h(p,T)-h_0(T)}{R} = \frac{a\alpha(T)\frac{\partial\alpha}{\partial T}}{RT\sqrt{8b^2}}\ln\left(\frac{2v_m+2b-\sqrt{8b^2}}{2v_m+2b+\sqrt{8b^2}}\right) - 1 + Z \qquad \text{Eq.28}$$

$$\frac{\partial\alpha}{\partial T} = -\frac{k\alpha(T)}{T_c T_r^{1/2}} \qquad \text{Eq.29}$$

3. EXPERIMENTAL CONDITIONS

The experiments [1] used for validation and

comparison with the numerical simulations detail the injection of transcritical and supercritical nitrogen into a quiescent nitrogen environment according to Tab. 2. The nitrogen pressure, p_∞, is considered constant at 4.0 MPa, while the injection velocity is 5 m/s. As described in Tab. 3 the pressure is kept above the critical point during the simulations, while the injection temperature ranges from supercritical conditions in case A to transcritical in case B. Accordingly, higher density gradients are expected in the transcritical injection cases as indicated in Tab. 3.

Table 2. Experimental conditions [1].

Case	p_∞ [MPa]	V_{inj} [m/s]	T_{inj} [K]	T_∞ [K]
A4	4.0	5.0	140	298
B4	4.0	5.0	118	298

Table 3. Non-dimensional experimental conditions [1].

Case	p_∞/p_c	T_{inj}/T_c	ρ_{inj}/ρ_c
A4	1.17	1.11	3.14
B4	1.17	0.84	12.5

The injector has a diameter of 1.9 mm and the chamber 100 mm. A length of 250 mm of the combustion chamber total length of 1 m is considered, decreasing computational cost, while ensuring a ratio of length to diameter high enough so that the region of interest is not affected by the outflow boundary condition (BC). On the other hand, the full length of the injector, 90 mm is considered, to ensure a fully developed turbulent flow at its exit plane. In the computations, the injector and chamber walls are considered isothermal [3] according to T_∞ while the injector faceplate is modelled as an adiabatic wall.

4. NUMERICAL MODELING

The finite volume method describes the integration of the system of partial differential governing equation into each control volume as defined by the grid. Each control volume is associated to a point in the mesh. The finite volume method has the advantage of automatically ensuring conservative discretization, which means that for two opposite cell-faces, the difference between both quantities is not dependent on the cell in which the face is considered.

A staggered grid configuration is used to ensure that the well-known odd-even decoupling of pressure and velocity does not happen, i.e., that pressure and velocity do not affect each other. Velocity and pressure values are stored in different positions for which the control volumes are no longer equal. Ultimately, the pressure values are calculated directly for the cell face, and no interpolation is needed. This eliminates the decoupling of the pressure and velocity fields, along with any possible oscillations. Diffusive fluxes in the governing equations are discretized by the second-order central scheme, while advective fluxes follow the QUICK scheme [17]. In this way, the appearance of non-physical pressure oscillations related to the formulation of the EoS and the transition across the Widom line is mitigated through the combination of the stability characteristic of central schemes with the directional behaviour of upwinding.
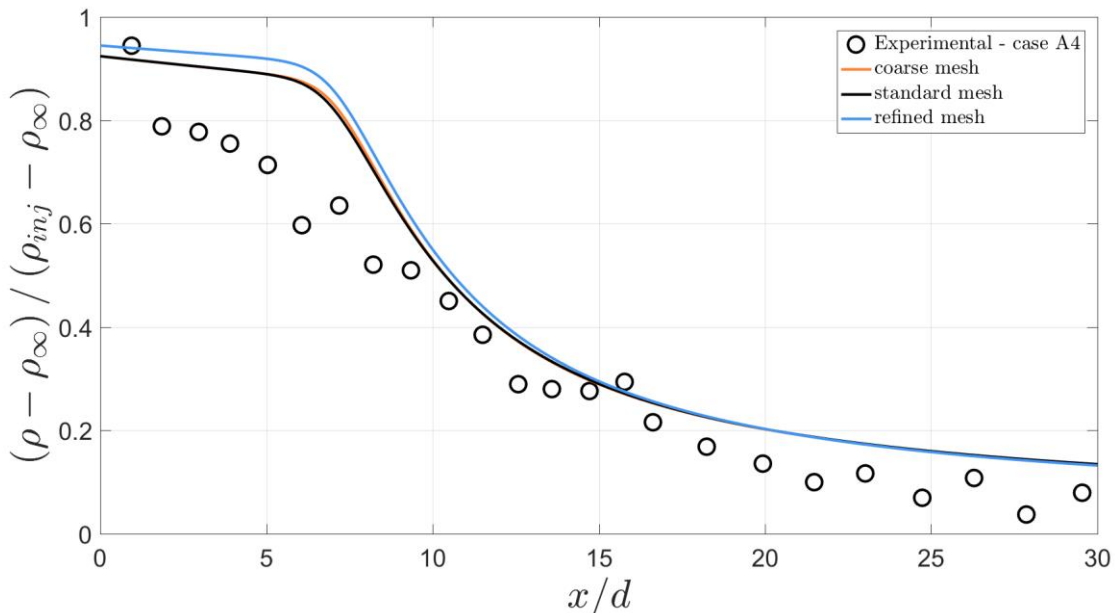

Figure 1. Grid refinement study considering the conditions of experimental test case A4.

5. VALIDATION

Fig.1 depicts a grid refinement study for experimental test case A4 considering three refinement levels: a coarse mesh with 180 000 points, a standard one with 280 000 points and a refined one with 495 000 points. The figure depicts

the normalized axial density distribution by the conditions at injection denoted by the index *inj* and chamber conditions by the index ∞ as a function of

the axial distance, *x*, measured from the injector exit plane normalized by the injector diameter *d*.
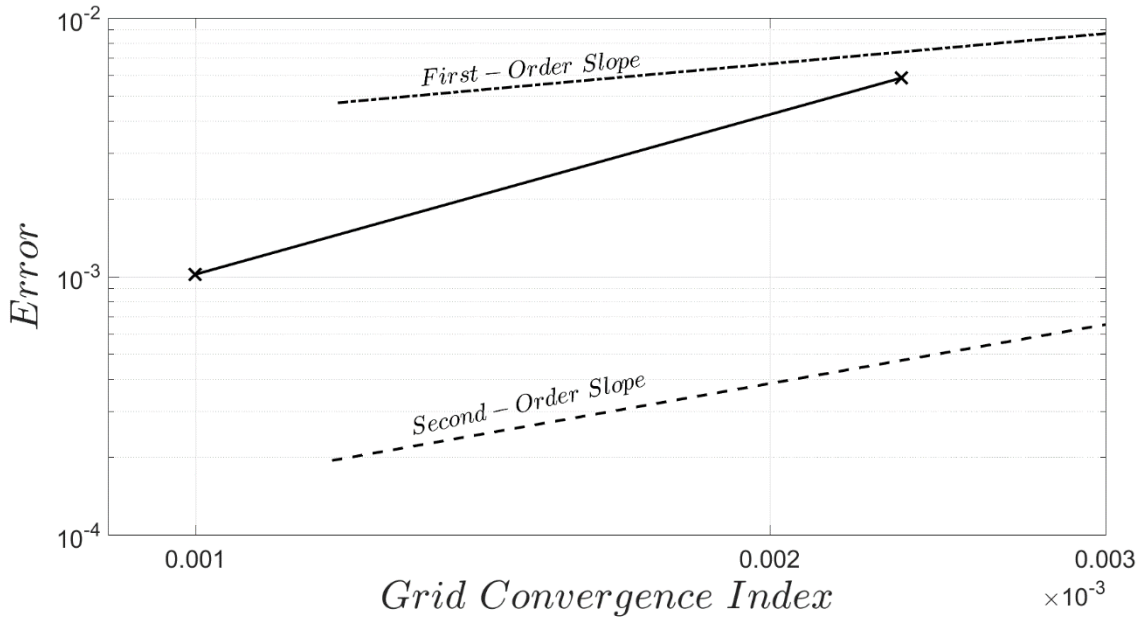

Figure 2. Evaluation of error as a function of the Grid Convergence Index.

In Fig.2 it is possible to observe the decrease in error for the grids of Fig.1 as we move from the coarser to the finer grid as a function of the grid convergence index [16]. The obtained slope indicates that as the grid is consecutively refined the error becomes smaller than second-order. An order of convergence of 2.512 is obtained versus the expected nominal rate of convergence of 3. Initial, boundary conditions, and the discrete representation of the continuous physical domain explain the difference between both values.

6. RESULTS

Fig. 3 depicts the comparison between the computations and the experimental data [1] in terms of density related information. In the top figure the non-dimensional axial density evolution of nitrogen is represented, defined according to Eq.30. The middle figure represents the full width at half maximum (FWHM) of density, a measure of the jet spreading rate, and the bottom figure represents the shape parameter, n_p for density, evaluated from Eq.31, giving a measure of the axial density shape profile. Axial density, FWHM of density and shape parameter are evaluated as a function of the non-dimensional distance measured from the injector exit plane, *x/d*.

$$\rho^* = \frac{\rho - \rho_\infty}{\rho_{inj} - \rho_\infty}$$ Eq.30

$$f\left(\frac{r}{r_m}\right) = \tanh^2\left[\left(\frac{r}{r_m}\right)^n\right]$$ Eq.31

The FWHM is a measure of the jet spreading, and it

is obtained by determining half the difference between the maximum and minimum values. The shape parameter, allows to quantify the characteristic shape of the density profile, where large values correspond to top hat-shaped profiles, and one relating to similarity profiles. All three quantities are depicted as a function of the normalized axial distance from the injector exit plane concerning its diameter and are compared against the experimental data indicated by the open circles.

The axial density evolution follows the experimental trend quite well. We can observe a decay until an *x/d* = 8. This is a consequence of the heat transfer in the injector, which is sufficient to trigger a pseudo-phase change from liquid to gas-like conditions; hence no potential core is observed. These results are accompanied by a good representation of the jet spreading. It is interesting to note that the jet starts to spread at *x/d* = 8, where the nitrogen in the chamber begins to entrain the jet, matching the mean density's sharper decay rate. Concerning the shape of the profile, we can infer that no similarity region is reached.

As expected, differences are observed concerning the results of the transcritical configuration in Fig.4. In the first section, until an x over d of 9.8, the transcritical jet evolves until the critical point value of temperature is reached, corresponding to a value of normalized density of 0.95, whose rate of decay is not retrieved from our model. After the critical point is surpassed, the liquid-like supercritical nitrogen will initially be unaffected by the conditions

in the chamber. However, the large density gradients, let me recall that the ratio between injectant and chamber density is 12.5 start to play a predominant role, with the fluid in the chamber entraining in the jet.

Looking into the jet spreading, we can observe a good prediction of jet growth, which we did not expect, considering that no two-phase flow model is present and the variations obtained in the mean axial density. Furthermore, concerning the previous case – case A4, we observe a lower jet growth per comparison. Lastly, no similarity profiles are obtained, as indicated by the shape parameter.
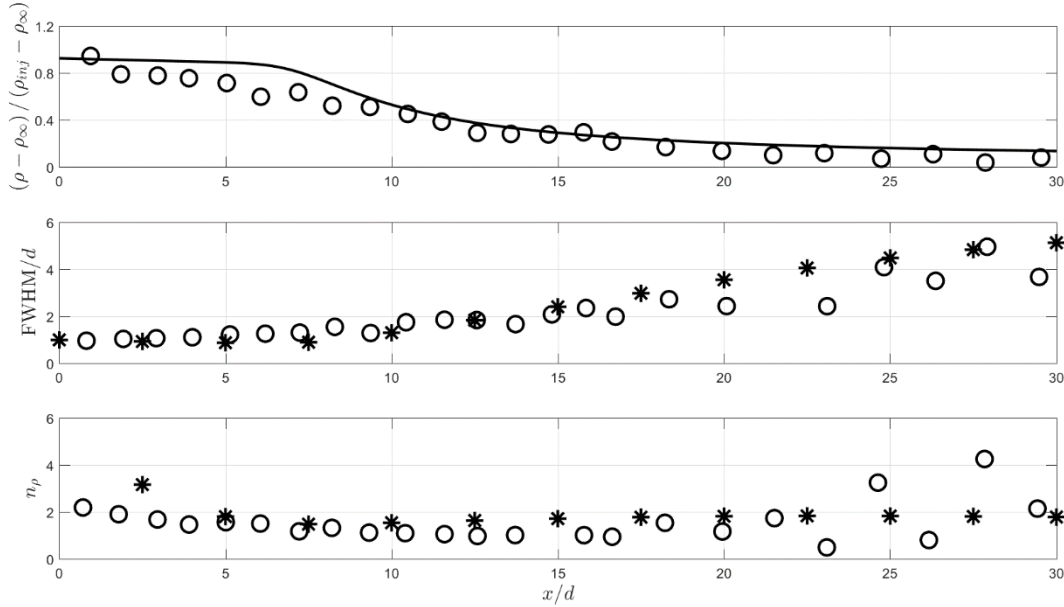
Figure 3. Comparison between density-related numerical results and experimental results for case A4 (top: axial density distribution; middle: Full Width at half Maximum of density; bottom: shape parameter). Lines and star symbols correspond to numerical results, while open circles represent experimental data.
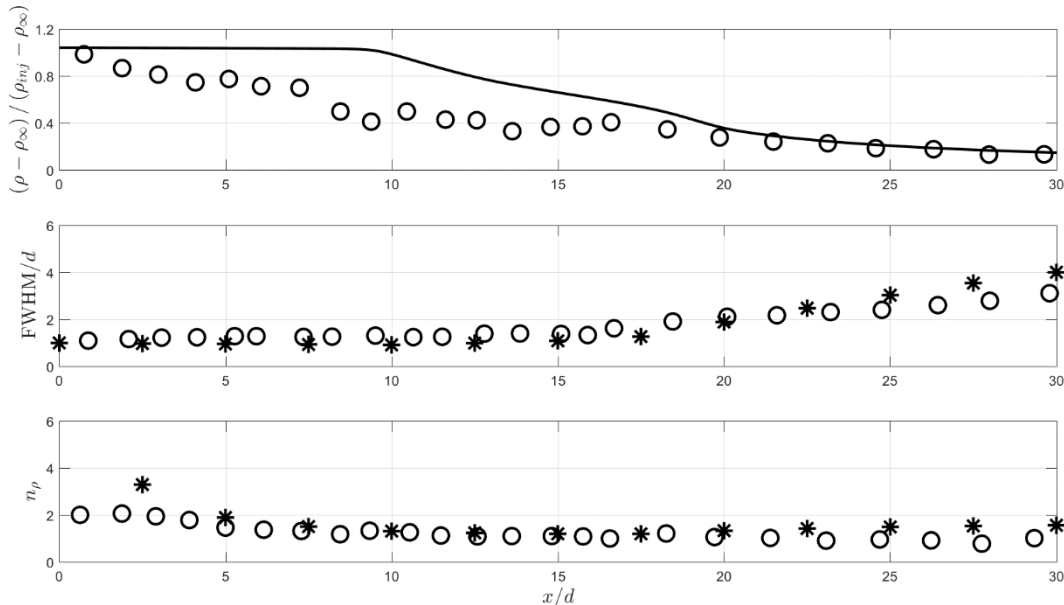
Figure 4. Comparison between density-related numerical results and experimental results for case B4 (top: axial density distribution; middle: Full Width at half Maximum of density; bottom: shape parameter). Lines and star symbols correspond to numerical results, while open circles represent experimental data.

7. CONCLUSIONS

In the proposed manuscript, we detailed on the validity of an incompressible variable density approach for the modelling of high-pressure fluid conditions, characteristic of liquid rocket engines operational range. Conditions of a single species high-pressure nitrogen experiment were selected

from the literature corresponding to transcritical and supercritical conditions, which were analysed in terms of the axial density evolution, FWHM of density and shape of the axial parameter.

A closer agreement between predictions and the experimental data was found for the supercritical jet of case A4 than for the transcritical one of case B4, in terms of the axial density evolution. We believe this to be due to the appearance of two-phase flow, in those conditions, which we did not account for in the model. Nevertheless, in terms of the transcritical jet spreading a similar agreement with the experimental data is reported for both supercritical and transcritical jets, which supports the hypothesis of incompressible but variable density approach as suitable to the be used in the modelling of jets at such conditions.

8. ACKNOWLEDGMENTS

9. REFERENCES

1. Banuti, D.T. (2015). Crossing the Widom-line – Supercritical Pseudoboiling. *J. Supercrit. Fluids* **98**(2015), 12-16.

2. Gerber, V., Baab, S., Förster, F.J., Mandler, H., Weigand, B. & Lamanna, G. (2021). Fluid Injection with Supercritical Reservoir Conditions. *J. Supercrit. Fluids* **169**(2021), 105097.

3. Oschwald, M. & Schik, A. (1999). Supercritical Nitrogen Free Jet Investigated by Spontaneous Raman Scattering. *Exp. Fluids* **27**(6), 497-506.

4. Barata, J., Gökalp, I., & Silva, A. (2003). Numerical Study of Cryogenic Jets under Supercritical Conditions. *J. Propuls. Power* **19**(1), 142-147.

5. Magalhães, L.B., Silva, A.R.R. & Barata, J.M.M. (2022). Contribution to the Physical Description of Supercritical Cold Flow Injection. The Case of Nitrogen. Acta Astronautica **190**(2022), 251-260.

6. Banuti, D. (2015). Thermodynamic Analysis and Numerical Modelling of Supercritical Injection. Ph.D. dissertation, Institute of Aerospace Thermodynamics University of Stuttgart.

7. Lapenna, P.E. & Creta, F. (2017). Mixing under Transcritical Conditions: An a Priori Study Using Direct Numerical Simulations. *J. Supercrit. Fluids* 128(2017), 263-278.

8. Schmitt, T., Rodriguez, J., Leyva, I.A. & Candel, S. Experiments and Numerical Simulation of Mixing under Supercritical Conditions. (2012). *Phys. Fluids* **24**(5), 55-104.

9. Unnikrishnan, U., Wnag, X., Yang, S. & Yang, V. (2017). Subgrid Scale Modeling of the Equation of State for Turbulent Flows under Supercritical Conditions. *53rd AIAA/SAE/ASEE Joint Propulsion Conference.* AIAA paper 2017-4855.

10. Okong'o, N. & Bellan, J. (2004). Perturbation and Initial Reynolds Number effects on Transition Attainment of Supercritical, Binary, Temporal Mixing Layers. *Comput. Fluids* **33**(8), 1023-1046.

11. Launder, B.E. & Spalding, D.B. (1972) Lectures in Mathematical Models of Turbulence, *Academic Press*, London, UK.

12. Peng, D. & Robinson, D.B. (1976). A New Two-constant Equation of State. *Ind. Eng. Chem. Fundam.* **15**(1), 59-64.

13. Lemmon, E.W. & Jacobsen, R.T. (2004). Viscosity and Thermal Conductivity Equations for Nitrogen, Oxygen, Argon and Air. *Int. J. Thermophys.* 25(1), 21-69.

14. McBride, B.J., Zehe, M.J. & Gordon, S. (2002). NASA Glenn Coefficients for calculating Thermodynamic Properties of Individual Species. *NASA Glenn Research Center.* Technical Report NASA/TP-2002-211556.

15. Reid, R.C., Prausnitz, J.M. & Poling, B.E. (1987). The Properties of Gases and Liquids. *McGraw-Hill, Inc.*

16. Roache, P.J. (1998). Verification and Validation in Computational Science and Engineering. *John Whiley & Sons*, Albuquerque, New Mexico.

17. Leonard, B.P. (1979). A Stable and Accurate Convective Modeling Procedure based on Quadratic Upstream Interpolation. *Appl. Mech. And Eng.* **19**(1), 58-98.